Finite Volume Particle Method for Fluid-Structure Interaction

Ebrahim Jahanbakhsh, Christian Vessaz, Audrey Maertens, François Avellan
Laboratory for Hydraulic Machines
École polytechnic fédérale de Lausanne (EPFL)
Lausanne, Switzerland
ebrahim.jahanbakhsh@epfl.ch, christian.vessaz@epfl.ch, audrey.maertens@epfl.ch, francois.avellan@epfl.ch

***Abstract*—We have recently developed a conservative finite volume particle method (FVPM) that can efficiently model 2-D and 3-D fluid flow with free-surfaces and complex geometries. Tn this paper we present an extension of the method to fluid-structure interaction. A new boundary condition enforcement is presented in which the hydrodynamic forces required in solid equations are computed directly. For validation, we study the 2-D motion of fluid through an elastic gate and compare the displacement of the gate with experimental and numerical data. We observe a very good agreement between FVPM and other numerical and experimental data.**

I. Introduction

The Finite Volume Particle Method (FVPM) is a particle-based method introduced by Hietel [1]. This method includes many of the desirable features of mesh-based finite volume methods. FVPM profits from particle interaction vectors to weight conservative fluxes exchanged between particles. In this methods, computational nodes are usually moving with material velocity which is compatible with the Lagrangian form of the motion equations. FVPM has some features of SPH but unlike SPH, it is locally conservative regardless of any variation in particle smoothing length. Quinlan and Nestor [2] proposed a method to compute the interaction vectors for 2-D cases exactly. Following their work, Jahanbakhsh [3] developed an exact FVPM applicable for 3-D cases. This method features the rectangular top-hat kernel and is implemented in SPHEROS software [4].

In this work, we employ weakly compressible flow equations to study viscous free-surface flows. To capture shock waves and discontinuities, AUSM$^+$ [5] is used to discretize the inviscid fluxes. Besides, the particles distribution is controlled by using *particle velocity correction* [6]. We also use linear elastic equation to compute solid material motion.

The volume-based formulation of FVPM intrinsically introduces the boundary conditions in the equations. Nestor et al. [6] enforce the boundary conditions by imposing appropriate constraints on the boundary fluxes. Their method is efficient, but can't be used for particles which are exposed to multiple boundary conditions *e.g.* free-surface and wall boundary. Recently, Quinlan et al. [7] computed the surface integral of the shape functions over the boundary. In that way, one can compute the interaction vector corresponding to each boundary condition individually. This method is precise and is applicable for complex boundaries. However, for 3-D cases, it induces costly geometrical operations which impact the performance of the method considerably. In this study, we introduce a new method to enforce the no-slip boundary condition by using fictitious boundary particles. In this method, a layer of fictitious particles are overlaid on the wall to enforce the boundary conditions. These fictitious boundary particles are governed by the fluid or solid equations except that their velocity is imposed. Using this approach, the interaction forces between fluid and solid phases are directly computed.

This paper is organized as follows. Section 2 describes the governing equations of weakly-compressible fluid flow and linear elastic solid material. In section 3, the FVPM formulation with rectangular top-hat kernel and exact computation of the interaction vector are summarized. The boundary conditions enforcement is presented section 4. Section 5 describes the implementation of the method, including inviscid flux computation, stresses tensor, smoothing mass flux, velocity correction. Finally, the validation of the new method is presented in section 6. For this purpose, fluid flow through an elastic gate is studied and the results are compared with numerical and experimental data.

II. Governing Equations

A. Elastic material

The elastic motion is governed by mass and linear momentum conservation equations

$$\frac{d\rho}{dt} = -\rho \nabla \cdot \boldsymbol{C} \tag{1}$$

$$\rho \frac{d\boldsymbol{C}}{dt} = \nabla \cdot \boldsymbol{\sigma} + \boldsymbol{f}_h + \rho \boldsymbol{g} \tag{2}$$

where $\frac{d}{dt}$ denotes substantial time derivative, ρ is the density, $\boldsymbol{C}$ is the velocity vector, $\boldsymbol{g}$ is the gravitational acceleration, $\boldsymbol{\sigma}$ is the Cauchy's stress tensor and $\boldsymbol{f}_h$ is the hydrodynamic forces exerted by fluid flow.

The rate of Cauchy's stress tensor, $\dot{\boldsymbol{\sigma}}$, is described by the Jaumann rate of stress, $\boldsymbol{\sigma}^{\triangledown}$

$$\dot{\boldsymbol{\sigma}} = \boldsymbol{\sigma}^{\triangledown} + \boldsymbol{\sigma} \cdot \dot{\boldsymbol{\omega}} + \dot{\boldsymbol{\omega}} \cdot \boldsymbol{\sigma} \tag{3}$$

where $\dot{\boldsymbol{\omega}}$ is the spin tensor defined as

$$\dot{\boldsymbol{\omega}} = \frac{\nabla \boldsymbol{C} - (\nabla \boldsymbol{C})^T}{2}. \tag{4}$$

For isotropic linear elastic material, Hookes's law reads

$$\boldsymbol{\sigma}^{\triangledown} = K\dot{\boldsymbol{\varepsilon}}_{vol} + 2G\dot{\boldsymbol{\varepsilon}}_{dev} \tag{5}$$

where K and G denote the bulk and shear modulus, respectively and $\dot{\boldsymbol{\varepsilon}}_{vol}$ and $\dot{\boldsymbol{\varepsilon}}_{dev}$ are defined as

$$\dot{\boldsymbol{\varepsilon}}_{vol} = \frac{1}{3}\mathrm{tr}\left(\dot{\boldsymbol{\varepsilon}}\right)\mathbf{I},$$
$$\dot{\boldsymbol{\varepsilon}}_{dev} = \dot{\boldsymbol{\varepsilon}} - \dot{\boldsymbol{\varepsilon}}_{vol} \tag{6}$$

in which, the deformation rate tensor, $\dot{\boldsymbol{\varepsilon}}$, reads

$$\dot{\boldsymbol{\varepsilon}} = \frac{\nabla \boldsymbol{C} + (\nabla \boldsymbol{C})^T}{2} \tag{7}$$

Substituting (5) into (3) yields

$$\dot{\boldsymbol{\sigma}} = 2G\dot{\boldsymbol{\varepsilon}}' + K\dot{\boldsymbol{\varepsilon}}_{vol} + \boldsymbol{\sigma}\cdot\dot{\boldsymbol{\omega}} + \dot{\boldsymbol{\omega}}\cdot\boldsymbol{\sigma}. \tag{8}$$

B. Fluid flow

Similar to the elastic material, the equations of motion for isothermal and weakly compressible flows are derived from the mass (1) and linear momentum conservation

$$\rho\frac{d\boldsymbol{C}}{dt} = \nabla\cdot(\boldsymbol{s} - p\mathbf{I}) + \rho\boldsymbol{g} \tag{9}$$

where p is the static pressure and $\boldsymbol{s}$ is the deviatoric stress tensor. For Newtonian fluids, $\boldsymbol{s}$ reads

$$\boldsymbol{s} = 2\mu\left(\dot{\boldsymbol{\varepsilon}} - \frac{1}{3}\mathrm{tr}\left(\dot{\boldsymbol{\varepsilon}}\right)\mathbf{I}\right) \tag{10}$$

where μ is the dynamic viscosity. To close the system of equations (1) and (9), an equation of state is required. The following equation of state is considered for water [8]

$$p = \frac{\rho_\circ a^2}{\theta}\left(\left(\frac{\rho}{\rho_\circ}\right)^\theta - 1\right) \tag{11}$$

where a is the speed of sound, $\rho_\circ$ is the reference density and θ is a constant coefficient. Here, we set $\theta = 7$. In weakly compressible flow simulations, the speed of sound a is considered at least ten times greater than the maximum fluid velocity to reduce the computational cost.

For convenience, we write the mass and momentum conservation equations in the form of a PDE arising from the conservation law

$$\frac{\partial \boldsymbol{U}}{\partial t} + \nabla\cdot\boldsymbol{F}\left(\boldsymbol{U}\right) = 0 \tag{12}$$

where $\boldsymbol{U} = \begin{pmatrix} \rho \\ \rho\boldsymbol{C} \end{pmatrix}$ represents the conserved variables and $\boldsymbol{F}$ represents the flux functions. For fluid and elastic equations, the corresponding flux functions are $\boldsymbol{F} = \begin{pmatrix} \rho\boldsymbol{C} \\ \rho\boldsymbol{C}\boldsymbol{C} - \boldsymbol{s} + p\mathbf{I} \end{pmatrix}$ and $\boldsymbol{F} = \begin{pmatrix} \rho\boldsymbol{C} \\ \rho\boldsymbol{C}\boldsymbol{C} - \boldsymbol{\sigma} \end{pmatrix}$, respectively.

III. Discretization

A. Finite Volume Particle Method

According to [3], the locally conservative form of FVPM equations reads

$$\frac{d}{dt}\left(\boldsymbol{U}_i V_i\right) = \sum_j \left(\boldsymbol{U}_{ij}\dot{\boldsymbol{x}}_{ij} - \boldsymbol{F}_{ij}\right)\cdot\boldsymbol{\Delta}_{ij} + \left(\boldsymbol{U}_b\dot{\boldsymbol{x}}_b - \boldsymbol{F}_b\right)\cdot\boldsymbol{B}_i. \tag{13}$$

where V_i is the volume of i^{th} particle and $\boldsymbol{U}_{ij}$ and $\boldsymbol{F}_{ij}$ are respectively the conserved variable and the flux at the interface of two particles. Moreover,

$$\dot{\boldsymbol{x}}_{ij} = \left(\dot{\boldsymbol{x}}_j\cdot\boldsymbol{\Gamma}_{ij} - \dot{\boldsymbol{x}}_i\cdot\boldsymbol{\Gamma}_{ji}\right)\frac{\boldsymbol{\Delta}_{ij}}{\boldsymbol{\Delta}_{ij}\cdot\boldsymbol{\Delta}_{ij}}, \tag{14}$$

$$\boldsymbol{\Delta}_{ij} = \boldsymbol{\Gamma}_{ij} - \boldsymbol{\Gamma}_{ji} \tag{15}$$

and

$$\boldsymbol{B}_i = -\sum_j \boldsymbol{\Delta}_{ij} \tag{16}$$

where $\dot{\boldsymbol{x}}_i$ is the velocity of i^{th} particle, which can be different from $\boldsymbol{C}_i$, and $\boldsymbol{\Gamma}_{ij}$ is the particles interaction integral which, for an arbitrary kernel function $W_i = W(\boldsymbol{x} - \boldsymbol{x}_i)$, reads

$$\boldsymbol{\Gamma}_{ij} = \int_\Omega \frac{W_i\nabla W_j}{\left(\sum_k W_k\right)^2} dV. \tag{17}$$

For fluid flows, we use density to compute the pressure field according to (11). To reach the particles density, as a part of conserved variables $\boldsymbol{U}_i$, we have to find V_i, the volume of i^{th} particle. The volume equation is derived as a special case of (13) using $\boldsymbol{U} = 1$ and $\boldsymbol{F} = 0$ and reads

$$\frac{dV_i}{dt} = \sum_j \dot{\boldsymbol{x}}_{ij}\cdot\boldsymbol{\Delta}_{ij} + \dot{\boldsymbol{x}}_b\cdot\boldsymbol{B}_i. \tag{18}$$

B. Rectangular top-hat kernel

For conventional bell-shaped kernels, the integral (17) is difficult or impossible to exactly evaluate. The alternative approach is to use quadrature rules which are approximate and costly [1], [6]. The computational needs of this approach have so far prevented the use of FVPM for 3-D applications. Recently, Quinlan and Nestor [2] have used top-hat kernels with circular supports for computing the integrals exactly and efficiently in 2-D. However, their exact FVPM does not readily generalize to 3-D and there is still no 3-D FVPM implementation yet. In order to extend the method to 3-D, Jahanbakhsh [3] used top-hat kernels with rectangular supports to compute the exact interaction vectors for 3-D case. Each particle is represented as a rectangular parallelepiped and any intersection results in a rectangular parallelepiped. Using rectangular top-hat kernels induces simpler geometric computations in comparison with spherical kernels and results in an efficient and precise method for 3-D cases.

The rectangular top-hat kernel is defined as

$$W_i\left(\boldsymbol{x}\right) = \begin{cases} 1 & \left\|\boldsymbol{x} - \boldsymbol{x}_i\right\|_\infty < h_i \\ 0 & \left\|\boldsymbol{x} - \boldsymbol{x}_i\right\|_\infty \geq h_i \end{cases}. \tag{19}$$

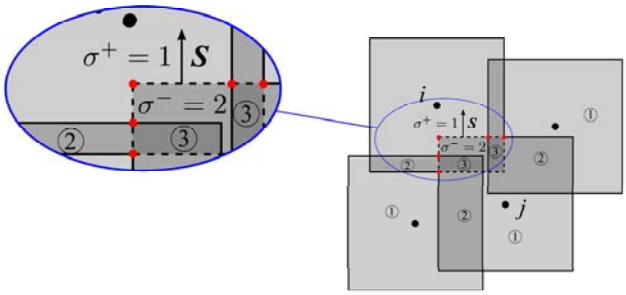

Fig. 1. Intersection volume of particles i and j is indicated by dashed line. $\Omega_i \cap \partial\Omega_j$ is broken into 4 partitions. σ^+, σ^- and area vector $\boldsymbol{S}$ are shown for a selected partition. The numbers inside the circles are the σ value of each zone.

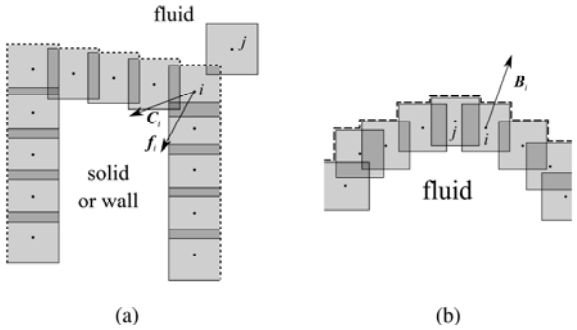

Fig. 2. (a) Boundary particles are distributed over the no-slip wall, indicated by dashed line. $\boldsymbol{C}_i$ denotes the imposed velocity for particle i. (b) Free surface boundary is indicated by dashed line and $\boldsymbol{B}_i$ denotes free-surface area vector for particle i.

Using (19), the supporting boundary of j^{th} particle, $\partial\Omega_j$, is split into m surfaces of constant kernel summation values and we can write

$$\boldsymbol{\Gamma}_{ij} = -\sum_{l}^{m} \left(\frac{\boldsymbol{S}_l}{\sigma_l^+ \sigma_l^-} \right) \tag{20}$$

where σ^+ and σ^- denote the kernel summations outside and inside of the $\partial\Omega_j$, respectively and $\boldsymbol{S}$ denotes the surface vector. Figure 1 depicts a representation of a 2-D system of particles in which the intersection border for particles i and j is broken into 4 partitions and the values for σ^+ and σ^- are shown for a selected segment.

For the 3-D case, the intersection zone is a rectangular parallelepiped whose facets are partitioned into rectangular surfaces. Definitions and the formula for the interaction vector do not differ from the 2-D case. However, special attention has to be paid in the surface partitioning process due to the complexity of 3-D geometries [3].

IV. Boundary conditions

To enforce the no-slip boundary condition for fluid flows, we overlay a layer of boundary particles that fits to the solid or elastic surfaces. These boundary particles artificially extend the fluid flow domain and prevent the fluid particles from crossing the boundaries. A schematic outline of the no-slip wall boundary particles with rectangular support is shown in Figure 2(a). Boundary particles are assumed like fluid. Their density is initially set to the fluid density $\rho_\circ$. These particles move with the wall velocity and their mass and volume are evolved according to the fluid governing equations (9) and (1). Finally, knowing the boundary particles density, their pressure is computed from the equation of state (11).

To enforce the displacement boundary condition for elastic material, we can employ the same approach as used for fluid flow no-slip wall boundary condition. In this case, elastic boundary particles are governed by elastic equations (2) and (1).

Both fluid and solid particles are exposed to the free-surface boundary. For the free-surface, no boundary particles are used. As shown in Figure 2(b), the free-surface is the union of the particles surfaces which have no interaction with other particles. The boundary interaction vector, $\boldsymbol{B}_i$, represents the area vector of the free-surface pointing outward. As discussed by Quinlan and Nestor [2], since we compute the interaction vectors exactly, $\boldsymbol{B}_i$ vanishes for interior particles. Free-surface is an impermeable boundary, meaning that the free-surface particle i obeys

$$(\dot{\boldsymbol{x}}_b - \boldsymbol{C}_b) \cdot \boldsymbol{B}_i = 0 \tag{21}$$

where index b denotes boundary values. Therefore, in (13), the convection terms $\begin{pmatrix} \rho_b \boldsymbol{C}_b \\ \rho_b \boldsymbol{C}_b \boldsymbol{C}_b \end{pmatrix}$, appearing in $\boldsymbol{F}_b$, are canceled by $\boldsymbol{U}_b \dot{\boldsymbol{x}}_b = \begin{pmatrix} \rho_b \dot{\boldsymbol{x}}_b \\ \rho_b \boldsymbol{C}_b \dot{\boldsymbol{x}}_b \end{pmatrix}$. Finally, setting the pressure and stresses to zero at the free-surface, the momentum flux at the free-surface becomes zero

$$(\boldsymbol{U}_b \dot{\boldsymbol{x}}_b - \boldsymbol{F}_b) \cdot \boldsymbol{B}_i = \boldsymbol{0}. \tag{22}$$

To enforce the free-surface boundary condition in volume equation (18), we define the free-surface velocity as that of the particle. Therefore, we can write

$$\frac{dV_i}{dt} = \sum_j \dot{\boldsymbol{x}}_{ij} \cdot \boldsymbol{\Delta}_{ij} + \dot{\boldsymbol{x}}_i \cdot \boldsymbol{B}_i. \tag{23}$$

The fluid particles are exerting hydrodynamic forces to the solid particles which are computed by

$$\boldsymbol{f}_i = \sum_{j \in \text{fluid}} (-p_{ij} \boldsymbol{I} + \boldsymbol{s}_{ij}) \cdot \boldsymbol{\Delta}_{ij} \tag{24}$$

where p_{ij} and $\boldsymbol{s}_{ij}$ are found based on the proposed no-slip wall boundary condition enforcement.

V. Implementation

In this study, we use the second-order explicit Runge-Kuta scheme for time integration. For numerical stability, the time step Δt is adapted as

$$\Delta t = \text{CFL} \times \min \left(\frac{h_i}{a + |\boldsymbol{C}_i|} \right) \tag{25}$$

With the FVPM, each particle interacts with its neighboring particles. Thus, at the beginning of each time-step, all particles

should identify their neighbors. Here, we employ incomplete-octree neighbor search algorithm [3], which features both efficiency and adaptivity.

To capture shocks and discontinuities in weakly-compressible flows, Riemann solvers are widely used to approximate the inviscid and pressure fluxes [9]. In this study, we use AUSM$^+$ to compute the inviscid and pressure fluxes at the interface particles. This method is an approximate Riemann solver, proposed by Liou [5], and can easily be extended to different types of equations of states. Following Nestor et al. [6], we employ the ALE-type extension of this method, presented by Luo et al. [10].

For elastic material, the stress tensor $\boldsymbol{\sigma}$ is stored at the interface of particles and the Cauchy's stress rate in (8) is directly computed at this point. Therefore, we avoid double summation gradient operators, which are prone to errors. To compute the stress at the interface between i and j, we need the velocity gradients. Here, we use the weighted least squares approach, *i.e.*

$$\begin{bmatrix} \tilde{f}(\boldsymbol{x}) \\ \tilde{\nabla} f(\boldsymbol{x}) \end{bmatrix} = \begin{bmatrix} \sum\limits_k \Phi_k & \sum\limits_k \Delta \boldsymbol{x}_k^{\mathrm{T}} \Phi_k \\ \sum\limits_k \Delta \boldsymbol{x}_k \Phi_k & \sum\limits_k \Delta \boldsymbol{x}_k \Delta \boldsymbol{x}_k^{\mathrm{T}} \Phi_k \end{bmatrix}^{-1} \begin{bmatrix} \sum\limits_k \Phi_k f_k \\ \sum\limits_k \Delta \boldsymbol{x}_k \Phi_k f_k \end{bmatrix} \tag{26}$$

where subscript k denotes the union of particles i and j neighbors, $\tilde{\nabla} f$ is the weighted least squares gradient of an arbitrary scalar field f at $\boldsymbol{x}$ and Φ_k is the Gaussian function defined as

$$\Phi_k(\boldsymbol{x}) = \exp\left(\frac{|\boldsymbol{x} - \boldsymbol{x}_k|^2}{h_k^2}\right). \tag{27}$$

Therefore, the spin tensor (4) and deformation rate tensor (4) are computed based on $\tilde{\nabla} \boldsymbol{C}_{ij}$.

In the fluid formulation, the pressure and velocity are computed at the same computational node. In this case, the coupling between velocity and pressure fields becomes weak and checker-board oscillations are likely generated [11]. Fatehi and Manzari [12] proposed a correction term for SPH method which is added to the mass equation and filters out the oscillations. We adapt this term to our formulation as

$$\boldsymbol{R}_{ij} = \left(\frac{\nabla p_i + \nabla p_j}{2} - \tilde{\nabla} p_{ij}\right) \Delta t \tag{28}$$

in which, ∇p_i is computed according to

$$\nabla p_i = \frac{\sum_j \left(\frac{p_i + p_j}{2}\right) \boldsymbol{\Delta}_{ij} + p_i \boldsymbol{B}_i}{V_i} \tag{29}$$

and $\tilde{\nabla} p$ is computed at the interface of particles i and j from (26). Finally, $\boldsymbol{R}_{ij} \cdot \boldsymbol{\Delta}_{ij}$ is added to the right hand side of the mass conservation equation (13).

The distribution of particles has a significant role in the control of the discretization error. FVPM is an ALE method, meaning that the particle velocity, $\dot{\boldsymbol{x}}$, can be prescribed arbitrarily. This feature, enables us to correct the particle velocity, such that a more uniform particle distribution is obtained. Following [6], we set the fluid particle velocity equal to the flow velocity $\boldsymbol{C}_i$, corrected with a correction vector $\dot{\boldsymbol{x}}_i'$

$$\dot{\boldsymbol{x}}_i' = -\lambda \left(\frac{h_i}{C^{\text{char}}}\right) \sum_j \frac{\Omega_{ij}'}{|\boldsymbol{\Delta}_{ij}|} \boldsymbol{n}_{ij} \tag{30}$$

where C^{char} is the characteristic velocity of the problem, Ω_{ij}' is the intersection of the bisected volumes of particles i and j, and λ is the adjusting parameter which is set to 0.5 in this study.

The correction vector, $\dot{\boldsymbol{x}}_i'$, is responsible for making the distribution of particles uniform and preventing the formation of clusters. To ensure the impermeability condition for the free-surface boundary, (21), the correction term is changed for free-surface particles. Therefore, the particle velocity reads

$$\dot{\boldsymbol{x}}_i = \begin{cases} \boldsymbol{C}_i + \dot{\boldsymbol{x}}_i' - \left(\dot{\boldsymbol{x}}_i' \cdot \boldsymbol{n}_i\right) \boldsymbol{n}_i & \text{for free-surface, } |\boldsymbol{B}_i| \neq 0, \\ \boldsymbol{C}_i + \dot{\boldsymbol{x}}_i' & \text{otherwise} \end{cases} \tag{31}$$

where $\boldsymbol{B}_i$ is given in (16) and $\boldsymbol{n}_i$ is the outward pointing unit vector at the free-surface

$$\boldsymbol{n}_i = \frac{\boldsymbol{B}_i}{|\boldsymbol{B}_i|}. \tag{32}$$

VI. Validation

In order to validate the proposed FVPM, we present an elastic gate test case to address key aspects of the method. We quantify the convergence rate of the method and verify the accuracy of the FVPM solution in 2-D computations by comparing with experimental and other numerical studies.

The experiment for this test case was conducted by Antoci et al. [13]. A schematic outline of the test case is depicted in Figure 3. The fluid tank is filled with water which is initially at rest. There is an elastic gate made of rubber on side of the tank. The elastic gate is fixed to the tank wall at the top and is free at the bottom. During the experiment, the elastic gate becomes open due to the hydrodynamic forces and the water flows through the gate. After a while, reducing the head of the water in the tank causes the elastic gate to return to the initial position. The displacement of the gate is a function of water hydrodynamic forces and the rubber elastic response. Therefore, the gate displacement time history can be used to verify the accuracy of the numerical method for fluid-structure interactions as well as the elastic behavior of the elastic material.

This test case was numerically studied by Antoci et al. [13], Lobovskỳ and Groenenboom [14] and Yang et al. [15]. The first two studies were performed using SPH-SPH method while the later one is done by a coupled SPH-FEM method.

The dimensions as well as the properties of the water and the rubber, used in this case are summarized as:

- The tank dimensions are $B = 0.1$ and $H = 0.14$ m.
- Elastic gate thickness is $S = 0.005$ m and its height is $L = 0.079$ m.
- Water density and viscosity are $\rho = 1000$ kg m^{-3} and $\mu = 0.001$ Pa s.
- Water sound speed is set to $a = 10$ m s^{-1}

- The rubber's Poisson's ratio and density are $\nu = 0.4$ and $\rho_s = 1100$ kg m^{-3}.
- The gravity acceleration is $\boldsymbol{g} = (0, -9.81)$ m s^{-2}

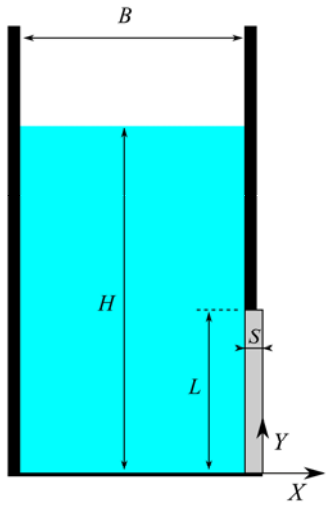

Fig. 3. Schematic outline of the elastic gate test case.

The interaction between the water and the elastic gate is enforced by the no-slip wall boundary condition. The no-slip boundary condition is also assumed for the water and the solid walls. The fluid, elastic and solid particles are uniformly distributed in the X and Y directions with the particle spacing of δ. The smoothing length of all particles is set to $h = 0.75 \times \delta$ and the time step is adapted with respect to CFL $= 0.5$.

As reported by Antoci [16], the experimental stress-strain curve for the rubber shows a nonlinear behavior (see Figure 4). However, due to the linear elastic hypothesis used in our formulation, we perform two sets of linear elastic simulations corresponding to two elastic modulus E_0 and E_{avg}, shown in Figure 4. The time histories of the X (solid line) and Y (dashed line) displacement of the elastic gate are shown in Figure 5 and 6 for $E = E_0$ and $E = E_{avg}$, respectively. As it is visible, the solutions are converged to the finest resolution solution. Figure 7, depicts the L_2-norm of the X displacement error as a function of particle spacing. The errors are computed with respect to the finest solution.

The displacement time histories of the elastic gate for $E = 10$ MPa and $E = 4$ MPa are shown in Figure 8 and 9, respectively. In Figure 8, the FVPM results are compared with the experimental data of Antoci et al. [13] and the linear elastic ($E = 10$ MPa) 2-D SPH-FEM results, studied by Yang et al. [15]. As it is visible, the FVPM results are in a very good agreement with the SPH-FEM solutions.

In Figure 8, the FVPM results are compared with the experiment [13] and the 2-D SPH-SPH results computed by Antoci et al. [13] and Lobovskỳ and Groenenboom [14]. In both [13] and [14], a linear elastic model with $E \approx 10$ MPa has been employed. For this case, a good agreement between FVPM and experimental data is observed.

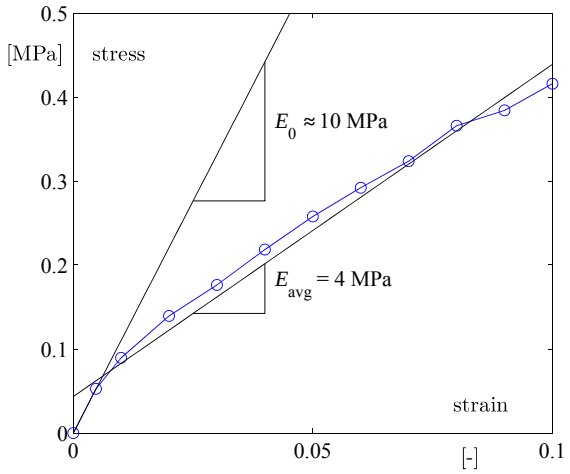

Fig. 4. Experimental stress-strain curve from [16].

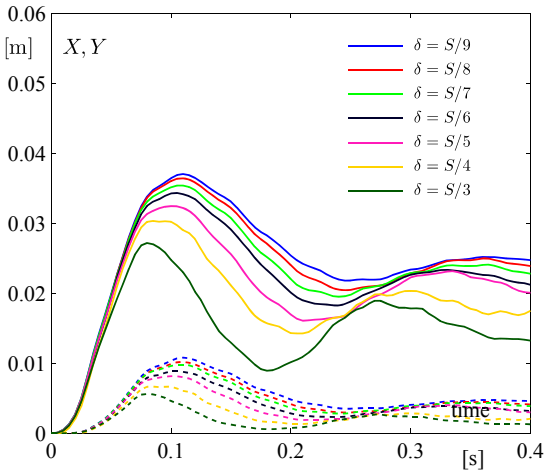

Fig. 5. Time history of the X (solid line) and Y (dashed line) displacement for the elastic gate with $E = 10$ MPa.

In Figure 8 which $E = 10$ MPa, despite the very good agreement between SPH-FEM and FVPM results, a considerable differences between experimental data and the numerical results are observed. The similar difference is reported for SPH-FEM studies performed in [15] and [17]. This difference is explained by the nonlinear behavior of the rubber in which the stiffness decreases as the strain increases. Nevertheless, using the average value for elastic modulus, $E_{avg} = 4$ MPa, results in a much better agreement between FVPM and experimental data (Figure 9).

The snapshots of the experiment [13] and the FVPM solution ($E = 4$ MPa) for different times are shown in Figure 10. The fluid particles in FVPM solution is colored by the pressure values. As we observe, the plate deformation and free surface position are well predicted for the five different times.

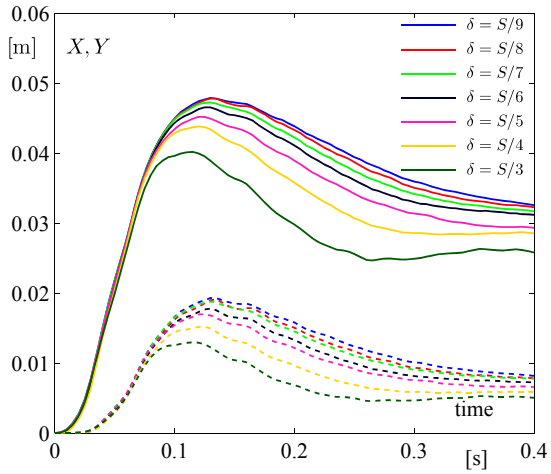

Fig. 6. Time history of the X (solid lone) and Y (dashed line) displacement for the elastic gate with $E = 4$ MPa.

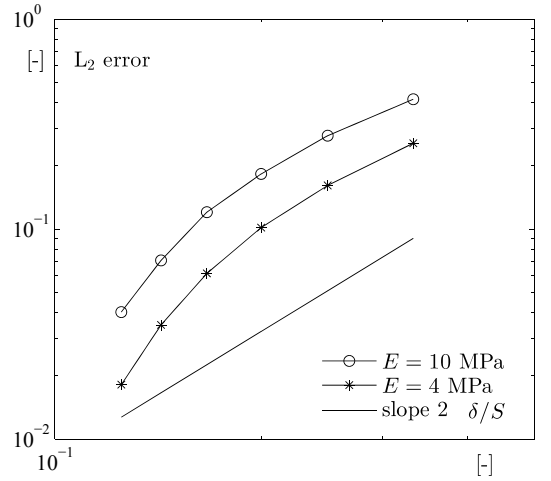

Fig. 7. The convergence of the L_2 norm of the X displacement error as a function of particle spacing.

VII. Conclusion

In this study, we proposed a FVPM formulation for fluid-structure interaction problems. In this formulation, the fluid particles are governed by weakly-compressible flow equations and the elastic rubber particles are governed by isotropic linear elastic equations. The interaction between fluid and solid is fulfilled by a new no-slip wall boundary condition which directly gives the hydrodynamic forces, required in solid equation. The particle interaction integrals are computed exactly by using rectangular top-hat kernels. The method is validated by an elastic gate test case. The convergence of the method was studied for different particle spacing. The FVPM results validated by a very good agreement with experimental and other numerical data.

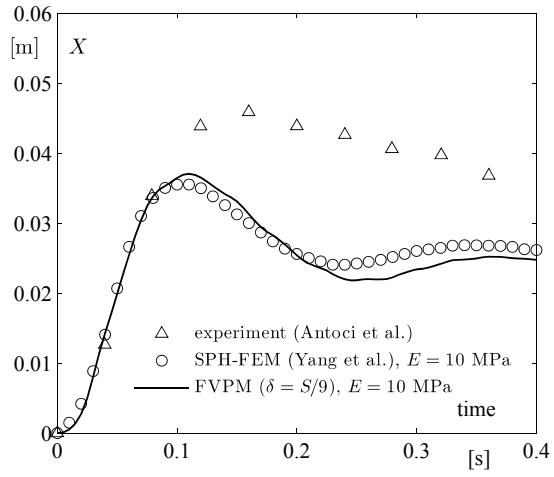

(a)

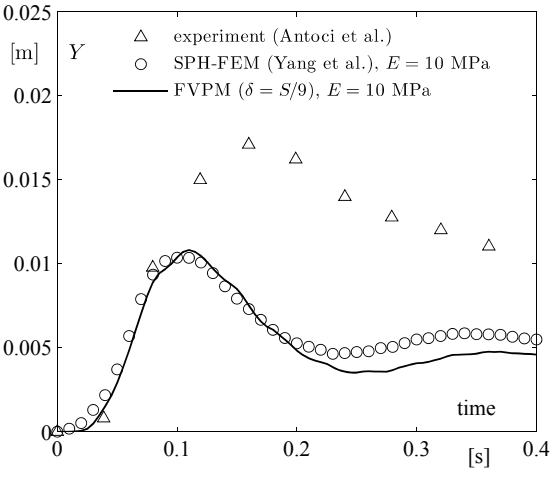

(b)

Fig. 8. Time histories for (a) X displacement and (b) Y displacement of the elastic gate. The FVPM results for $E = 10$ MPa are compared with the experimental data of Antoci et al. [13] and SPH-FEM solution of Yang et al. [15].

Acknowledgment

The research leading to the results published in this paper has received funding from both SCCER SoE, the Swiss Energy Center for Energy Research Supply of Electricity, granted by the Swiss Commission for Technology and Innovation (CTI), and the Ark, the foundation for innovation of Valais Canton, through the Project HydroVS.

The authors would like also to acknowledge the financial support and technical assistance of ALSTOM Power Hydro for the development of the SPHEROS software.

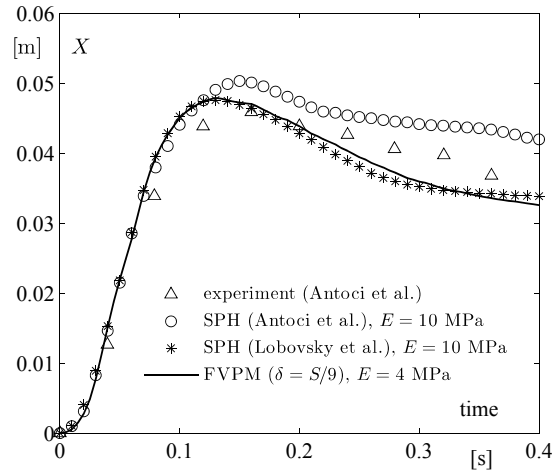

(a)

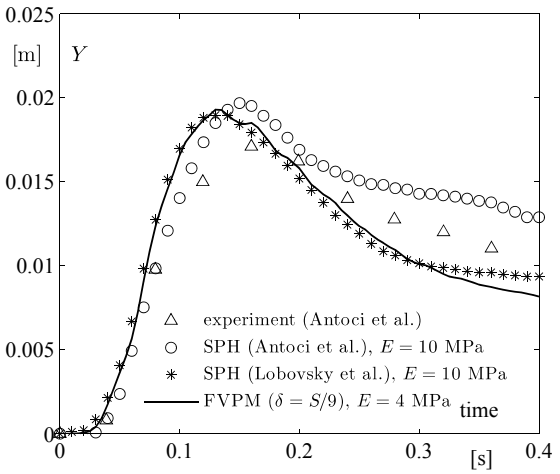

(b)

Fig. 9. Time histories for (a) X displacement and (b) Y displacement of the elastic gate. The FVPM results for $E = 4$ MPa are compared with the experimental data of Antoci et al. [13] and SPH solution of Antoci et al. [13], [13] and Lobovskỳ and Groenenboom [14].

REFERENCES

[1] D. Hietel, K. Steiner, and J. Struckmeier, "A finite-volume particle method for compressible flows," *Mathematical Models and Methods in Applied Sciences*, vol. 10, no. 9, pp. 1363–1382, 2000.

[2] N. J. Quinlan and R. M. Nestor, "Fast exact evaluation of particle interaction vectors in the finite volume particle method," in *Meshfree Methods for Partial Differential Equations V*. Springer Berlin Heidelberg, 2011, pp. 219–234.

[3] E. Jahanbakhsh, "Simulation of silt erosion using particle-based methods," Ph.D. dissertation, École Polytechnic Fédéral de Lausanne, 2014.

[4] E. Jahanbakhsh, O. Pacot, and F. Avellan, "Implementation of a parallel SPH-FPM solver for fluid flows," *Zetta Numerical Simulation for Science and Technology*, vol. 1, no. 1, pp. 16–20, 2012.

[5] M.-S. Liou, "A Sequel to AUSM: AUSM$^+$," *Journal of Computational Physics*, vol. 129, no. 2, pp. 364 – 382, 1996.

[6] R. M. Nestor, M. Basa, M. Lastiwka, and N. J. Quinlan, "Extension of the finite volume particle method to viscous flow," *Journal of Computational Physics*, vol. 228, no. 5, pp. 1733–1749, 2009.

[7] N. J. Quinlan, L. Lobovsk, and R. M. Nestor, "Development of the meshless finite volume particle method with exact and efficient calculation of interparticle area," *Computer Physics Communications*, vol. 185, no. 6, pp. 1554 – 1563, 2014.

[8] C. Vessaz, E. Jahanbakhsh, and F. Avellan, "Flow Simulation of Jet Deviation by Rotating Pelton Buckets Using Finite Volume Particle Method," *ASME. Journal of Fluids Engineering*, vol. 137, no. 7, pp. 74 501–74 501, 2015.

[9] E. F. Toro, *Riemann solvers and numerical methods for fluid dynamics : a practical introduction*. New York: Springer Berlin Heidelberg, 2009.

[10] H. Luo, J. D. Baum, and R. Lhner, "On the computation of multi-material flows using ALE formulation," *Journal of Computational Physics*, vol. 194, no. 1, pp. 304 – 328, 2004.

[11] J. H. Ferziger and M. Peric, *Computational methods for fluid dynamics*, 3rd ed. Springer, 2002.

[12] R. Fatehi and M. T. Manzari, "A consistent and fast weakly compressible smoothed particle hydrodynamics with a new wall boundary condition," *International Journal for Numerical Methods in Fluids*, vol. 68, no. 7, pp. 905–921, 2012.

[13] C. Antoci, M. Gallati, and S. Sibilla, "Numerical simulation of fluid-structure interaction by SPH," *Computers & Structures*, vol. 85, no. 1114, pp. 879 – 890, 2007, fourth MIT Conference on Computational Fluid and Solid Mechanics.

[14] L. Lobovskỳ and P. H. Groenenboom, "Smoothed particle hydrodynamics modelling in continuum mechanics: fluid-structure interaction," *Applied and Computational Mechanics*, vol. 3, pp. 101 – 110, 2009.

[15] Q. Yang, V. Jones, and L. McCue, "Free-surface flow interactions with deformable structures using an SPH-FEM model," *Ocean Engineering*, vol. 55, pp. 136 – 147, 2012.

[16] C. Antoci, "Simulazione numerica dell interazione fluido-struttura con la tecnica sph," Ph.D. dissertation, Università di Pavia, 2006.

[17] L. Lobovskỳ and P. H. Groenenboom, "Remarks on FSI simulations using SPH," in *Proceedings of the 4th international SPHERIC workshop, Nantes*, 2009, pp. 379–384.